Short fatigue crack growth mechanism in Ni-Co based superalloy at elevated temperatures and in oxidative atmospheres

Hideaki Nishikawa, Kishan Habib, Yoshiyuki Furuya, Toru Hara, Toshio Osada, Kyoko Kawagishi

Affiliation

Research Center for Structural Materials (RCSM), National Institute of Materials Science (NIMS), 1-2-1 Sengen, Tsukuba 305-0047, Japan

Corresponding author:

Hideaki Nishikawa

e-mail: NISHIKAWA.Hideaki@nims.go.jp

Abstract

In this study, to elucidate the oxidation effect on the short fatigue crack growth (SFCG) characteristics of Ni-Co based TMW-4M3 superalloy, fatigue tests were conducted at room/elevated temperature in air/vacuum and three-dimensional microscopic observation of the SFCs using a plasma focused ion beam – scanning electron microscope (PFIB – SEM) system. Fatigue lives tested under vacuum at elevated temperature were comparable to those at room temperature while those tested at elevated temperatures in air showed shorter fatigue life in higher stress regions and longer fatigue life in lower stress regions

than the others. *In situ* observation of SFCs at elevated temperatures in air revealed SFCG deceleration in the small ΔK regions and acceleration in large ΔK regions. SFCs opening/closing behaviours at elevated temperatures measured by digital image correlation (DIC) showed the crack opening stress to be higher at elevated temperature in air, possibly due to oxide-induced crack closure. However, the crack closure effect did not fully explain the difference in FCG rate between room and elevated temperatures in air. Three-dimensional investigations revealed SFCs to form at elevated temperatures in air, showing straight transgranular FCG to be insensitive to microstructure in slow growth regions, and intergranular FCG to precede that in the surrounding material in fast growth regions, in contrast to microstructural SFCs features at room temperature. It appears that slow and straight unique SFCG at elevated temperatures might occur due to intermittent brittle fracture of oxides formed at the crack tip. This suggests a possible role of the oxide layer at the crack tip in broadening the plastic deformation distribution, thus contributing to FCGR deceleration.

Keywords: Ni-Co based superalloy, Elevated temperature, oxidation, Short fatigue crack, Crack closure, Three-dimensional observation, PFIB-SEM

1. Introduction

γ′-strengthened polycrystalline Ni-based superalloys are in wide use for turbine disks in advanced aircraft engines and land-based gas turbines, owing to their superior mechanical properties at elevated temperatures, specifically their tensile, creep and fatigue properties [1]. Many types of advanced disk superalloys have also been developed for further improvement of fuel efficiency. We have previously proposed a novel design concept for a Ni-Co based superalloy based on a combination of Ni-based superalloys and Co-based alloys with γ- γ′ two-phase structures [2–4]. A series of cast-and-wrought Ni-Co based superalloys (TMW alloys) developed based on this concept has been reported to have excellent phase stability [5], and better tensile and creep properties [2,4,6,7] than conventional Alloy720Li superalloy. They are therefore anticipated to have major potential for use in next-generation turbine disks.

Fatigue failure is one of the most important failure modes that must be considered in the design of aerospace structures, especially in cyclically loaded aircraft engines [8,9]. Investigation of high-temperature fatigue failure, including small crack growth behaviour, will be the key to the safe design of rotating turbine discs, which are life-limited parts with advanced safety requirements [9].

Zhong et al. [10–13] reported that fatigue crack growth rates (FCGRs) increased with increasing temperature due to oxidation-assisted grain boundary cracking. However, it is crucial to gain an understanding of the microscopic initiation and propagation behaviour of short fatigue cracks (SFCs), which

usually grow faster than macroscopic fatigue cracks [14]. Even though short fatigue crack growth (SFCG) tends to account for more than 60 % of total fatigue life [15], is difficult to describe it in terms of fracture mechanics theory due to other effects that include microstructural heterogeneity, large-scale yielding conditions, and unsteady-state crack closure [14]. Hence, an understanding of short fatigue crack growth behaviour can lead to a more accurate awareness of the causes of fatigue life variation.

In recent advanced lifing methods applied to aero gas turbines, fatigue crack initiation and growth life have been evaluated individually, employing non-linear analysis [9]. Using this method, 'engineering' crack initiation life usually includes microscopic fatigue crack growth life. Hence, an appropriate understanding of SFCG behavior at elevated temperatures will be a key contributor to the accuracy of fatigue life evaluation of aero gas turbines. It is also necessary to clarify the effects of oxidation to be able to understand SFCG at elevated temperatures. There are currently only a few investigations into SFCG behaviour at elevated temperatures [16–21] for superalloys because of impediments to their observation. Their results successfully demonstrated the acceleration of SFCs at elevated temperatures. Grain-boundary cracking due to oxidation has also been pointed out [22]. However, little remains known of SFCG characteristics at elevated temperatures. One key item to be elucidated is the effects of oxidation on crack closure, which has also been noted in a previous review paper [23], from the perspective of oxidation-induced crack closure [24].

It is necessary to investigate the SFCG mechanism at elevated temperatures from the mechanical and metallurgical perspective.

In this study, to clarify the effects of oxidation on the SFCG characteristics of TMW-4M3 superalloy, fatigue tests were carried out under vacuum and in air at elevated temperatures. SFC growth and its opening/closing behaviors at RT and elevated temperatures were directly observed using an in-house-developed microscope system in conjunction with digital image correlation (DIC) [25]. Furthermore, aiming to clarify the SFCG path, three-dimensional details of SFCs were investigated using a plasma focused ion beam - scanning electron microscope (PFIB-SEM) system.

2. Material and experimental procedure

2.1 Material preparation

The material used in this study was TMW-4M3, a Ni-Co based superalloy that had been fabricated using a conventional cast-and-wrought processing route, including triple melting, billet making, and high-temperature forging, at Proterial Ltd., Japan (formerly Mitsubishi Materials Corporation, Japan). The details of the methods can be seen elsewhere [4]. The chemical composition of the alloy is given in Table 1. A pancake-shaped disk (440 mm in diameter and 65 mm in thickness), fabricated by forging, was subjected to solution heat treatment at below the γ′-solvus temperature (1120 ˚C/4 h oil quenching), followed by two-

step aging heat treatment (650 ˚C/24h/air cooling + 760 ˚C/16h/air cooling). The mechanical properties at elevated temperatures are shown in Table 2.

2.2 Initial microstructure

Figure 1 shows microstructural images of TMW-4M3 superalloy. In the alloy, multiple strengthening mechanisms via hierarchical microstructure successively come into play and enhance its high-temperature mechanical properties. As can be seen in Figs. 1 a) to d), the alloy is strengthened by boundary strengthening via grain and annealing twin boundaries; precipitation strengthening due to primary, secondary, and tertiary γ′ precipitates; and solid solution strengthening via multiple alloying elements. Small amounts of MC-type carbide were also observed on grain boundaries (Fig. 1 b)). All the microstructural features are summarized in Table 3. Here, grain size was measured excluding annealing twin boundaries. Further, two types of grain size are also listed in Table 3. One is an area average, which is average obtained by multiplying the diameter of each grain by the area of the grains, and the other is a number average, in which is the sum of all the grain diameters divided by the total number. Further, note that grain size also included some of the primary γ′ precipitates with a coherent γ/γ′ interface.

2.3 Fatigue testing procedure

Fatigue specimens were fabricated from the heat-treated pancake-shaped disk. Specimen configurations are shown in Figure 2. The three types of specimens: type A for conventional fatigue testing and B and C for microscopic *in situ* observation, were prepared. The specimen surfaces were mechanically polished with emery paper, followed by buff polishing to obtain a mirror surface. The hatched area of the type B and C specimens for surface observation shown in Fig. 2 b) and c), were subsequently etched. A small notch was created using focused ion beam (FIB) milling at the centre of all specimens as the fatigue crack starter.

Figure 3 shows the experimental setups for fatigue tests. They were performed in air and under vacuum at RT and elevated temperatures. Normal axial load fatigue testing at 650 ˚C was conducted in air and under vacuum below 1 x 10^{-2} Pa at a loading frequency of 20 Hz. Microscopic *in situ* fatigue crack growth observations were performed at RT and at 500 ˚C in air with a loading frequency of 20 Hz and 5 Hz respectively. Both fatigue tests were conducted using a servo-hydraulic fatigue testing machine under axial load-controlled conditions at a stress ratio of –1. The specimen's temperature was controlled using a heat induction coil and thermocouples attached to the specimen's surface. The specimen's temperature had been previously calibrated using thermocouples welded to the specimen's centre and shoulder.

The SFCs growth and opening/closing behaviour was observed using an in-house-developed automatic *in situ* microscope observation system, as described in our previous paper [25]. The system comprises a fatigue testing machine, a digital microscope and an electric three-axis stage with a programmable logic controller (PLC). The specimen surfaces were observed thorough the heat induction coil using this system. The fatigue test was suspended at regular intervals of numbers of cycles, and the observation system was used to automatically focus on and capture a series of high-magnification panoramic images of the specimen surface. For the crack opening stress evaluation using DIC analysis, 40 images were captured from minimum to maximum load at each panoramic position, and for all the regular intervals of number of cycles. The image captured at the minimum load at that position was used as the reference image for the DIC.

DIC analysis was conducted using commercially available analysis software (VIC-2D, Correlated Solutions), employing 8-bit images of 1600 × 1200 pixels (0.41 μm/pixel) captured using a digital microscope (VHX5000, Keyence) [25] Microstructural features of the alloy visible after etching were used as patterns for DIC analysis. The conditions for DIC analysis were set in the range of 61 - 67 pixels for the subset size and 7 pixels for the step size.

The long fatigue crack growth tests at room temperature were also conducted according to ASTM E647 at a load ratio of 0.05, using a compact tension (CT) specimen of W = 50 mm, B = 10 mm, obtained from the same forged disk. Crack

opening stress was evaluated using the 1 % compliance offset method described in ASTM E647, using a back face strain gauge.

The initial microstructure was evaluated using scanning electron microscopy (SEM), scanning ion microscopy (SIM) and electron backscatter diffraction (EBSD) analysis. Energy dispersive X-ray spectrometry (EDS) was performed to observe the oxides formed during the fatigue test.

Three-dimensional observation of SFCs that had propagated at RT and at 500 ˚C in air were conducted using the PFIB-SEM system. The targeted volume measured about 200 x 80 x 70 μm and took the form of a rectangular parallelepiped. Serial sectioning observation was carried out under the following conditions: 1,000 images were recorded every 100 nm slice and EBSD patterns were taken every five slices. More details of the 3D analysis procedure are given in our previous report [26].

A total of 5 types of fatigue test conditions were summarized in Table 4.

Table 1. Nominal alloy composition (wt.%) of TMW-4M3

Alloy	Ni	Co	Cr	Mo	W	Al	Ti	C	B	Zr
TMW-4M3	Bal.	25.0	13.5	2.8	1.2	2.3	6.2	0.015	0.015	0.03

Table 2. Mechanical properties of TMW-4M3

Temperature (˚C)	0.2 % proof strength (MPa)	Tensile strength (MPa)	Elongation (%)	Reduction of area (%)	Young's modulus (GPa)
RT	1165	1615	13	14	230
400	1080	1537	12	12	212
650	1048	1421	14	15	194
700	1046	1270	13	12	190
750	1008	1132	9	10	185

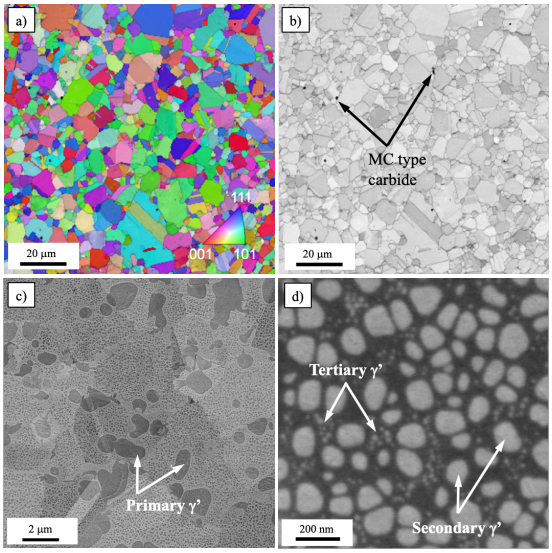

Figure 1. Microstructure images of TMW-4M3: (a) Inverse pole figure (IPF) map; (b) Image quality (IQ) map including MC type carbides on grain boundaries; (c) SEM image showing primary γ′; and (d) SEM image showing secondary and tertiary γ′ precipitates within γ-grains.

Table 3. Typical microstructural features in TMW-4M3 Ni-Co based superalloy

Grain size (μm)		Primary γ′ phase		Secondary γ′ phase		Tertiary γ′ phase		MC type carbide	
Area average	Number average	Volume fraction	Size (μm)	Volume fraction	Size (nm)	Volume fraction	Size (nm)	Volume fraction	Size (μm)
10.7 ± 8.51	3.77 ± 3.15	0.153	3.56 ± 1.27	0.326	95.2 ± 25.6	0.020	16.5 ± 5.6	< 0.005	~5-10

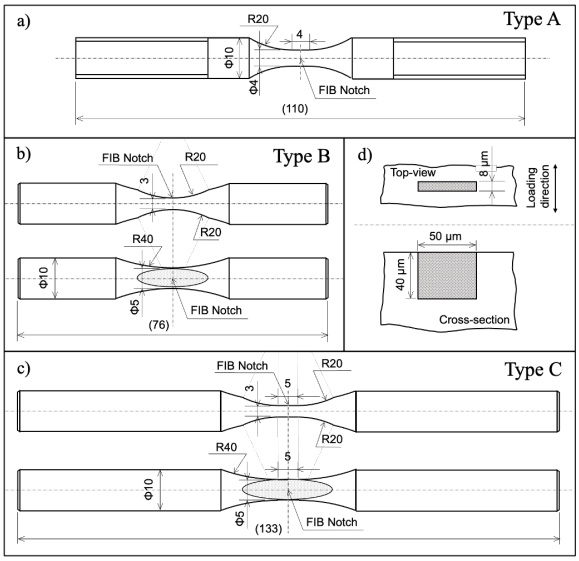

Figure 2. Fatigue specimen configurations for a) normal axial load fatigue testing, b), c) for *in situ* observations at RT and at elevated temperatures. A small FIB notch, shown in d), was cut into all the fatigue specimens to act as a crack starter.

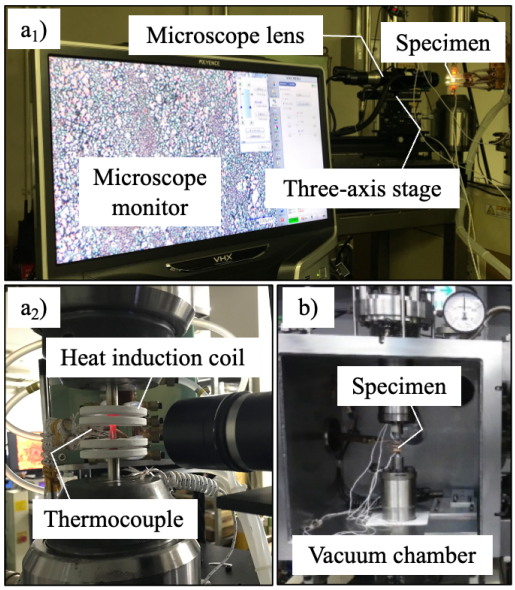

Figure 3. Experimental setups of a) *in situ* observation and b) fatigue testing under vacuum.

Table 4 List of fatigue test conditions

No.	Environment	Temperature	Specimen	Evaluated crack	Crack closure measurement	Load ratio	Frequency
1	Air	650 ˚C	Type A	-	-	-1	20 Hz
2	Vacuum	650 ˚C	Type A	-	-	-1	20 Hz
3	Air	RT	Type B	Short crack	DIC	-1	20 Hz
4	Air	500 ˚C	Type C	Short crack	DIC	-1	5 Hz
5	Air	RT	CT specimen	Long crack	Back face strain gage	0.05	20 Hz

3. Results

3.1 S-N diagram and fracture surface

Figure 4 shows the S-N diagram of the TMW-4M3 superalloy at RT and elevated temperatures. All the specimens have a small FIB notch of 50 μm length cut into them. Hence the fatigue lives are roughly considered to be the fatigue crack growth life. The fatigue lives at 650 ˚C under vacuum were comparable to those performed at RT in air. The fatigue lives at elevated temperatures in air were shorter than the others, although the fatigue limit was higher. Note that the fatigue lives in air at 650 ˚C and 500 ˚C were comparable. It appears that the effects of temperature alone on SFCG behaviour were relatively minor, whereas oxidation at elevated temperatures affected SFCG behaviour.

Figure 5 shows typical fracture surfaces. Figure 5 a) shows one at 500 ˚C in air. As shown in Fig. 5 a2), the surface looks flat up to a depth of around 150 μm from the bottom of the notch. Intergranular fracture surfaces are observed in deeper regions, as shown in Fig. 5 a3). In contrast, microstructural facets are shown in Fig. 5 b2) and c2), showing RT in air and 650 ˚C under vacuum respectively.

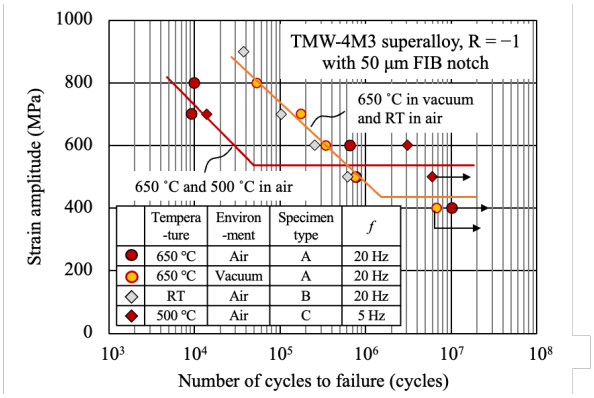

Figure 4. S-N diagram of the TMW-4M3 superalloy at RT and elevated temperatures

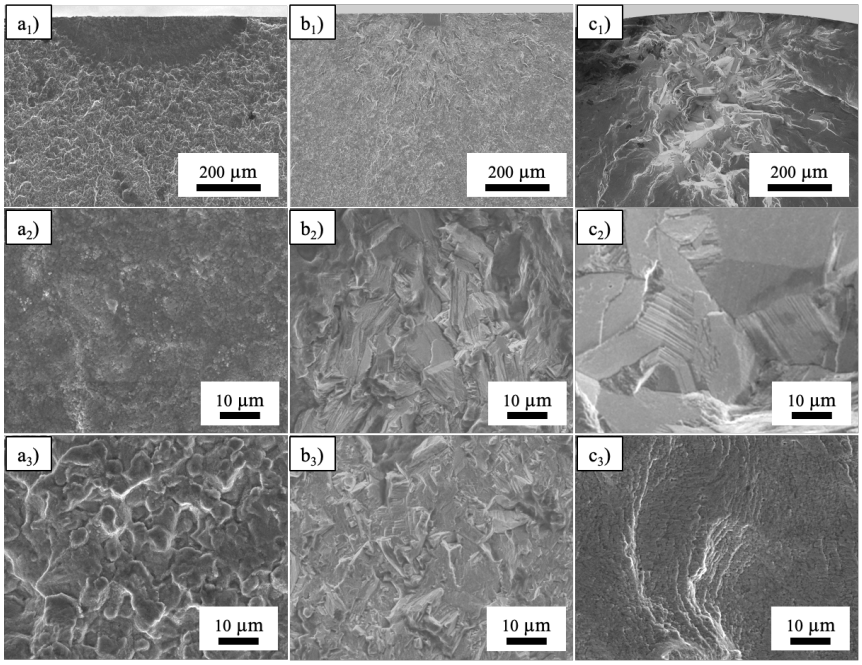

Figure 5. Typical fracture surface images for a) 500 ˚C in air, b) RT in air and c) 650 ˚C under vacuum, tested at σ_a = 600, 900 and 600 MPa respectively. a1), b1) and c1) show overviews; a2), b2) and c2) shows an enlarged area at 0.1 mm from the crack initiation region; a3), b3) and c3) shows an enlarged area 0.3 mm distant from the crack initiation region.

3.2 Short fatigue crack growth behaviour at RT and elevated temperatures

The microscopic SFCG behaviour of 500 ˚C and RT in air were investigated to clarify the effects of oxidation. Figure 6 shows typical microscopic images of the SFCs observed at RT and 500 ˚C. White arrows show the crack tip positions of each image. The SFCG behaviour at elevated temperatures was clearly observed using our digital microscope system. The SFCG at RT shows a zigzag path while that at 500 ˚C follows almost a straight across the grains until a crack length of around 0.3 mm, where is marked by dotted arrows in Fig. 4 b), after which the crack growth takes on a zigzag path. These SFCs appearance corresponded to the fracture surface morphology shown in Figure 5.

Figure 7 shows the crack growth curves at different stress amplitudes, measured using our *in situ* microscope system. Most of the fatigue lives of the specimens were consumed by fatigue crack growth life, regardless of temperature or stress amplitude. Figure 7 a) shows the fatigue crack growth curves at a stress amplitude of 700 MPa. The SFCG life at 500 ˚C is considerably shorter than that at RT, and the SFCG rate at 500 ˚C was faster than at RT. Figure 7 b) and c) respectively show the curves at the stress amplitudes of 600 MPa and 500 MPa. The SFCG lives at 500 ˚C are significantly longer than those at RT. The fatigue crack growth rate of the last part of the fatigue test under 600 MPa showed sudden acceleration. A non-propagating fatigue crack was also observed at high temperatures and at a stress amplitude of 500 MPa, as shown in Figure 7 c). The non-propagating fatigue crack length was about 0.2 mm.

Figure 8 shows cross-sectional SEM and EDS images observed at about 20 μm from the FIB notch. As shown in Fig. 8 b), the oxide layer was observed just below the fracture surface tested at 500 ˚C.

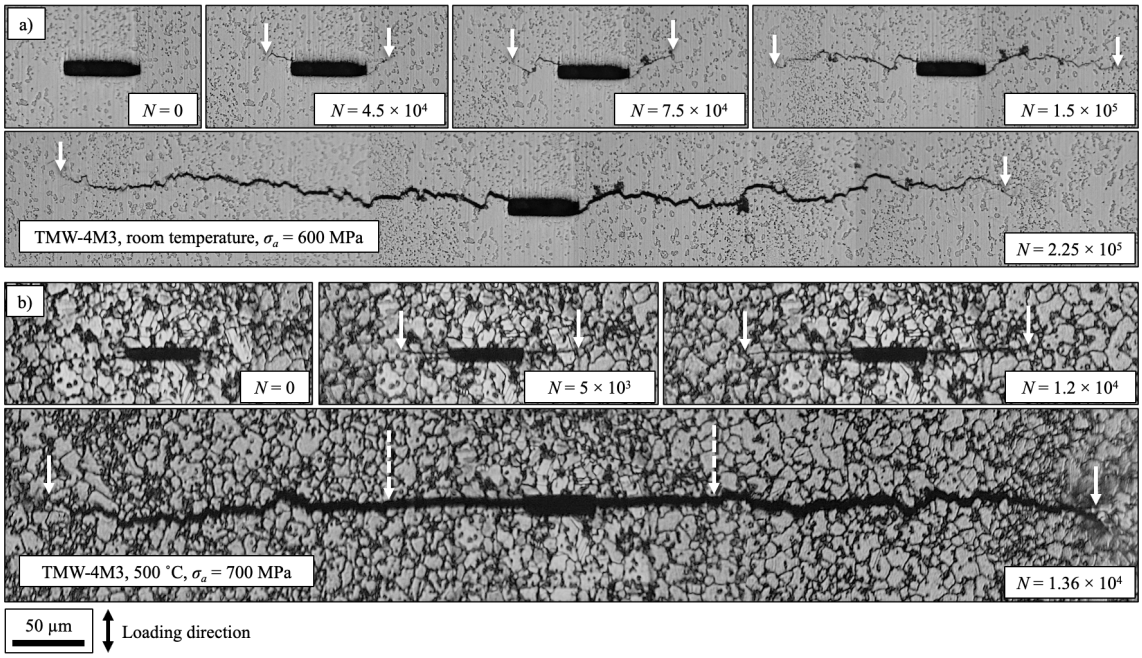

Figure 6. Typical microscopic images of the SFCs observed at a) RT and b) 500 ˚C, tested at σ_a = 600 and 700 MPa respectively.

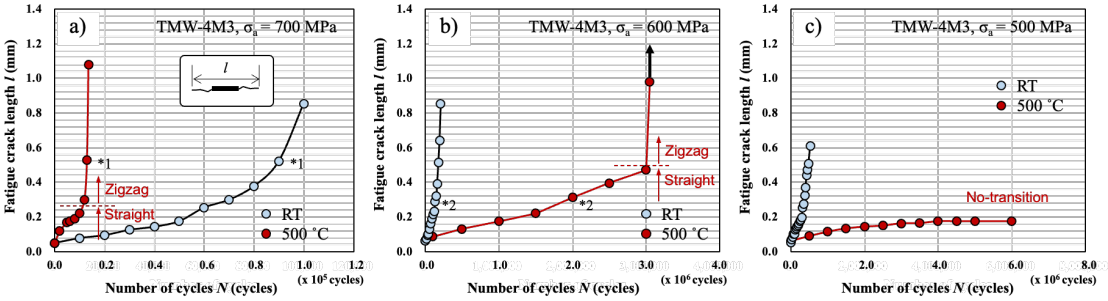

Figure 7. SFC growth curves at RT and 500 ˚C tested in air. Crack opening/closing behaviour measured at the point of *1 and *2 in the Figure were represented in Fig. 10 and 11 respectively

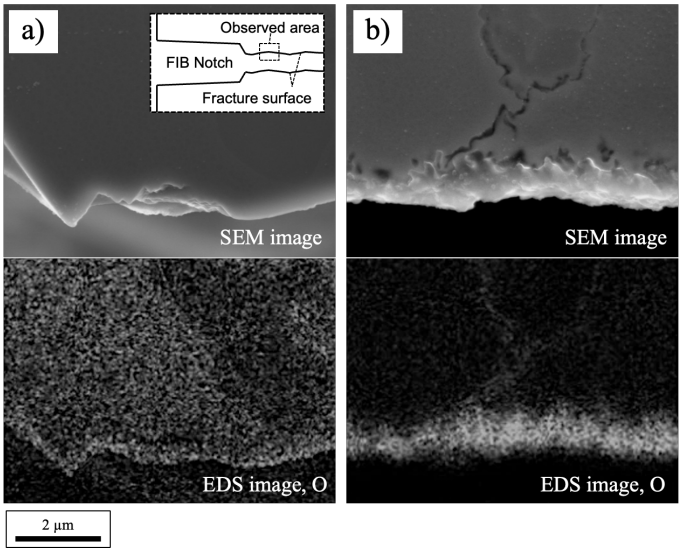

Figure 8. Cross sectional SEM and EDS mapping images of oxide for a) RT and b) 500 ˚C tested at σ_a = 600 MPa in air, measured near the crack origin

3.3 Effects of oxidation on SFCs' opening/closing behaviour

It is well known that oxidation enhances crack closure; it is termed oxide-induced crack closure. The opening and closing behaviors of SFCs at elevated temperatures were directly measured using the same DIC technique as previously applied to the SFCs at room temperature [25,27,28]. Figure 9 shows an example of the opening behaviour of SFCs at elevated temperatures, analyzed using the DIC technique. The strain contours in the vertical direction, calculated using DIC, are represented. When the crack opens, the apparent strain increases due to crack opening displacement. The gradually opening behavior of the crack during the loading part was successfully visualized by DIC. As shown in Fig. 9, the crack tip region did not open at stresses of under 90 MPa, whereas it appears to have opened at 360 MPa.

Figures 10 and 11 shows crack closure curves that were evaluated by unloading elastic compliance of the crack opening displacement (COD) measured at 50 μm behind of the crack tip. Figure 10 shows measurements under conditions in which the FCGR was accelerated at elevated temperatures, with Fig. 11 for contrast. Measurements show FCGR to decelerate at elevated temperatures. Crack opening points were determined according to the 6 % compliance offset method which is described in the appendix of ASTM E647 [29]. As shown in Fig. 10, the effective stress range, which is the range between maximum stress and crack opening stress at RT and elevated temperatures were comparable at 600 MPa and 700 MPa respectively. In contrast, the effective

stress range at RT in Fig. 11 was 66 % greater than that at elevated temperatures. Figure 12 shows crack opening stress to be a function of crack length. Those at elevated temperatures at 500 MPa and 600 MPa were higher than that at room temperature, especially when the crack was small.

Figure 13 shows SFCs' growth rate represented with a) ΔK and b) ΔK_{eff}. The long cracks FCGR obtained using CT specimens and of those reported in previous research [10,30] are simultaneously represented in the Figure. The SFCs growth rate at RT was in fairly close agreement with that of long cracks by using the effective stress intensity factor range, whereas it did not match that of FCGR at elevated temperatures. SFCs' growth trend at elevated temperatures appears to have a transition point of around ΔK_{eff} = 5 - 7 MPa $m^{0.5}$. This transition point also roughly corresponded to the changing point of the fracture surface of the flat area to the intergranular cracking area shown in Figure 4.

Based on the above evaluation, although the oxide-induced crack closure appears to be one of the deceleration factors in the small ΔK region, it was not sufficient to explain the difference in FCGR between room and elevated temperatures.

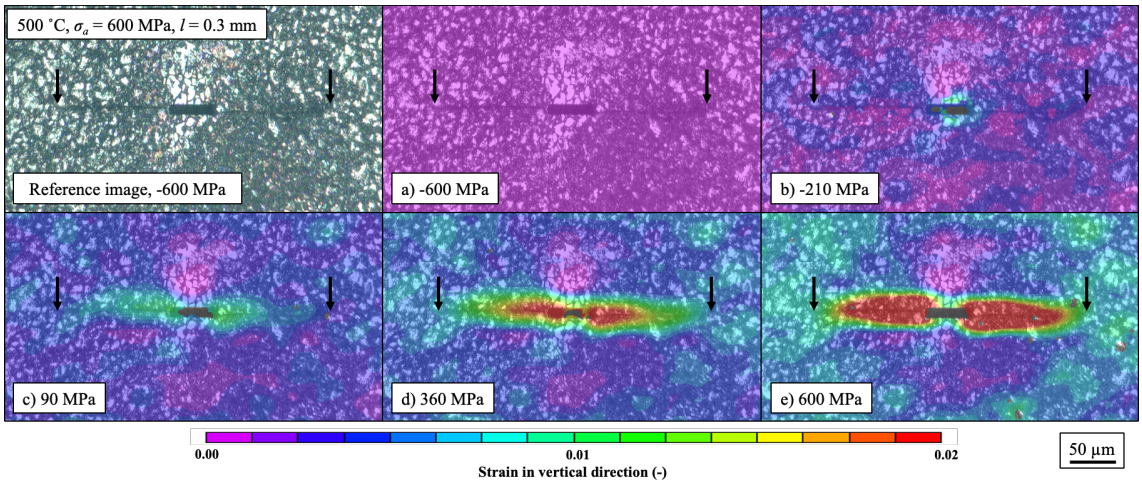

Figure 9. An example of the directly observed opening behaviour of SFCs at elevated temperatures, analyzed using DIC. Black arrows indicate crack tip positions. The image captured timings of a) to e) correspond to those indicated in Figure 11 b).

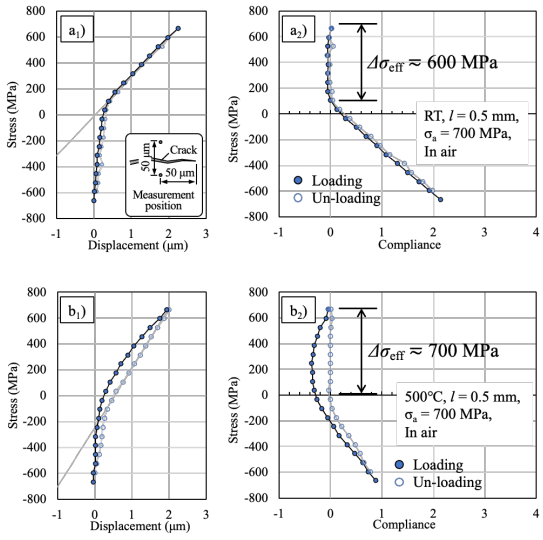

Figure 10. Crack closure curves of SFCs at a) RT and b) at 500 ˚C, measured where the FCGR accelerated at elevated temperatures corresponding to point *1 marked in Figure 7.

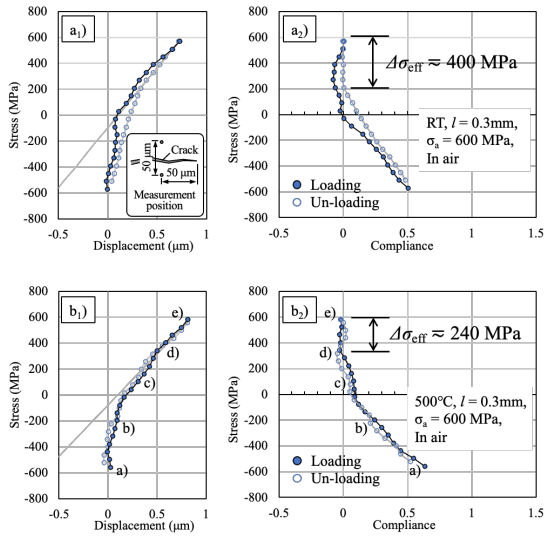

Figure 11. Crack closure curves of SFCs in a) RT and b) 500 ˚C, measured where the FCGR decelerated at elevated temperatures, corresponding to point *2 marked in Fig. 7.

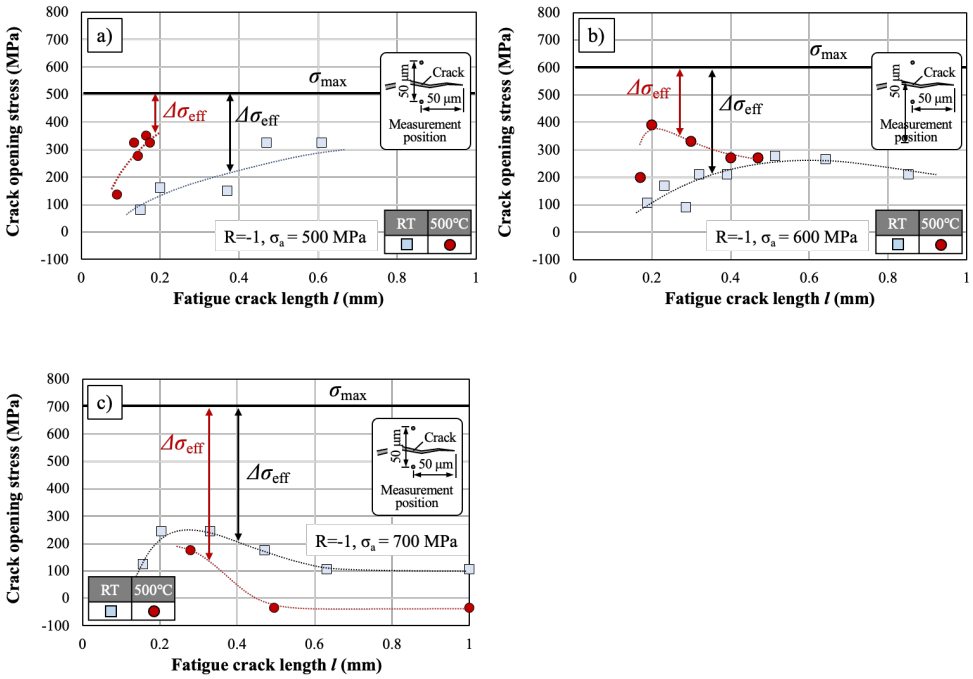

Figure 12. Crack opening stress versus surface crack length at a) σ_a = 500 MPa, b) σ_a = 600 MPa and c) σ_a = 700 MPa.

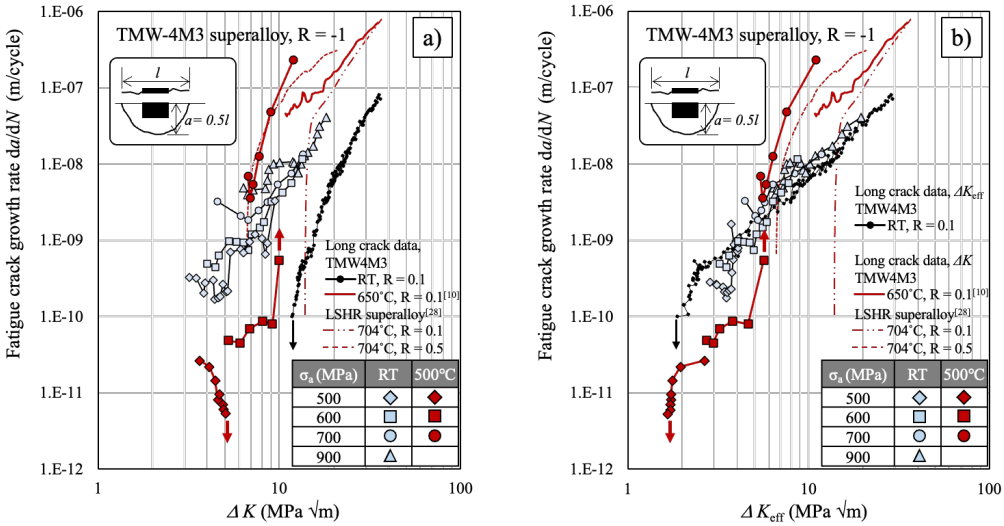

Figure 13. SFC growth rates represented by a) ΔK and b) ΔK_{eff} corrected with crack opening stress measured by DIC.

3.4 Three-dimensional evaluation of SFCs morphologies

Three-dimensional fatigue crack morphologies at room and elevated temperatures were investigated using the PFIB – SEM serial sectioning technique [26] to elucidate the features of microscopic fatigue crack growth.

Figure 14 shows the three-dimensional SFCs morphologies at a) RT and b) 500 ˚C. Figure 15 shows a stereographic projection of the pole figure which corresponds to Fig. 14 a2) and b2). Three-dimensional observation results for the SFCs at RT of Fig. 14 a) were reported in ref. [26]. As described in this previous report, SFCs' growth path at room temperature mainly corresponded to the {111} slip plane of the FCC, as shown in blue in Fig. 14 a_2), which corresponds to the

four {111} peaks in Fig. 15 a). Hence, a large part of the crack surface was declined from the loading axis as shown in Fig. 14 a_3).

In contrast, almost flat, non-crystallographic features of the crack path were observed in the SFCs at 500 ˚C. As shown in Fig. 14 b2) and Fig. 15 b), no crystallographic textures could not be observed. The crack growth direction was close to perpendicular to the loading axis, as shown in Fig. 14 b_3). In addition, crack growth paths along the grain boundaries of relatively small grain sizes were observed. These are marked in red in Fig. 14 b_4). The intergranular crack precedes the surroundings, but crack s that were completely isolated from the main crack were not observed. Figure 16 shows typical grain reference orientation deviation (GROD) maps at RT and 500 ˚C where the crack is propagating inside of the grain. The apparent plastic zone was more broadly distributed at 500 ˚C than at RT.

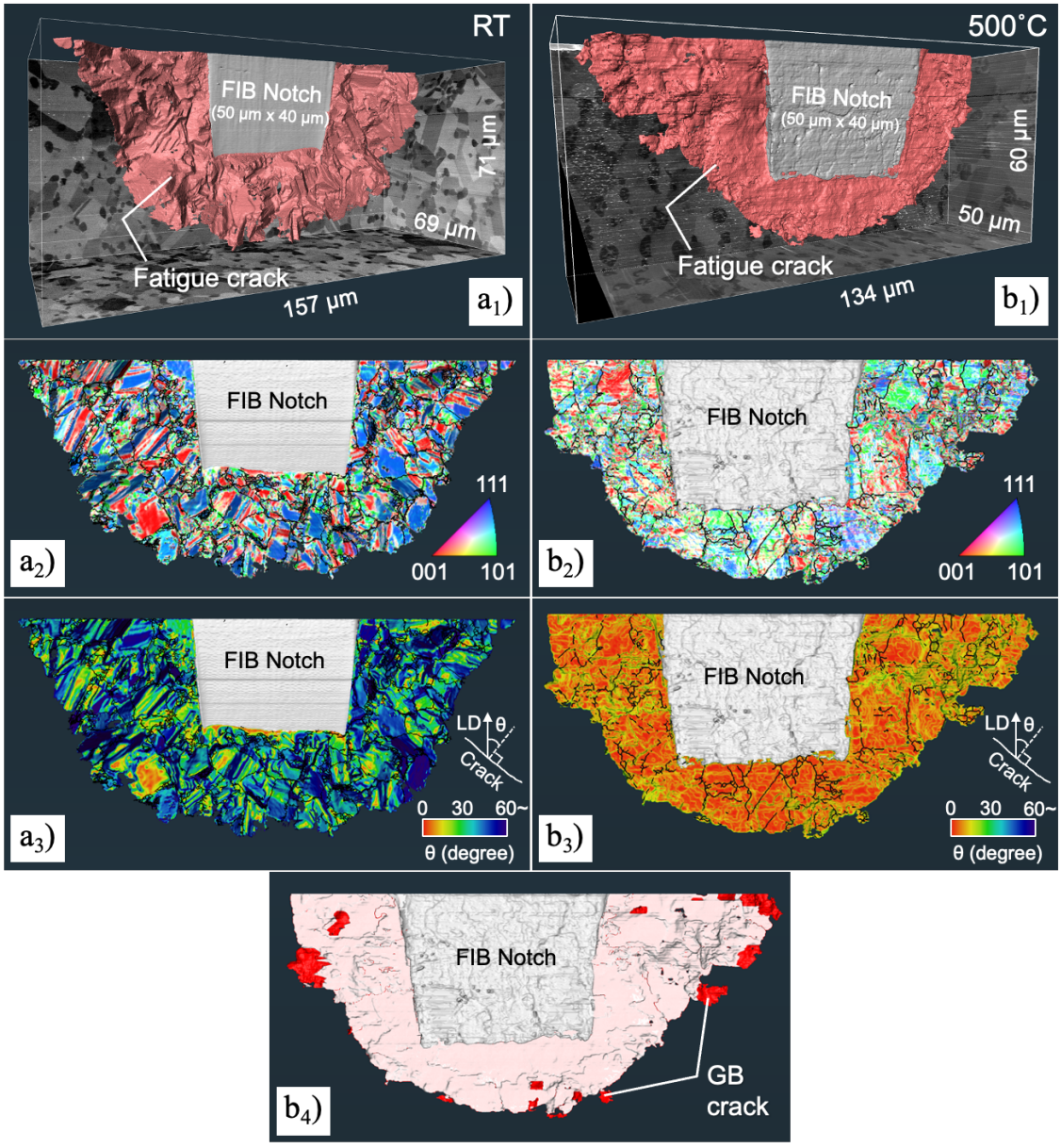

Figure 14. Three-dimensional SFCs morphologies of a) RT and b) 500 ˚C: Images a1) and b1) shows overviews of SFCs; the crystal orientation of crack growth path is represented in a2) and b2). The crack angle from the loading axis is shown in a3) and b3); the crack paths that clearly correspond to the grain boundaries are represented as red areas in b_4). The stress amplitudes at RT and 500 ˚C were 900 MPa and 700 MPa respectively.

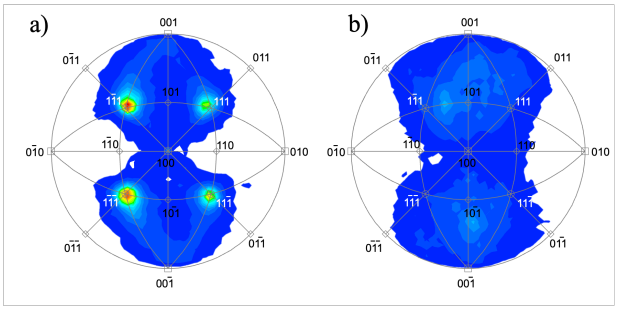

Figure 15. Stereographic projection of pole figure for a) RT and b) 500 ˚C corresponding to Fig. 14 a2) and b2).

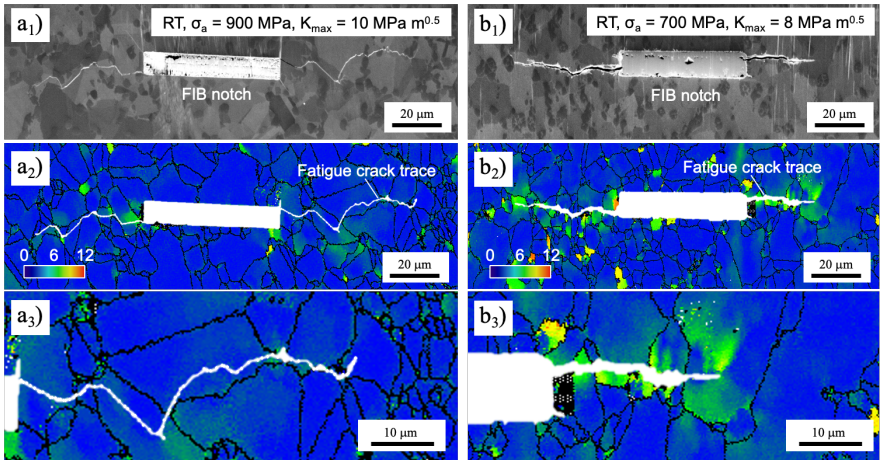

Figure 16. GROD map around the crack at a) RT and b) 500 ˚C captured at 10 µm below the specimen surface. *ΔK* values at the crack tip were 10 and 7.3 MPa $m^{0.5}$ respectively.

4. Discussion

The fatigue tests carried out in this study revealed the negative and positive effects of oxidation on the fatigue properties of Ni-Co based TMW-4M3 superalloy. The intergranular (IG) fracture mode appeared in the fast FCG region and flat transgranular (TG) fractures appeared in the slow FCG region. To achieve an accurate understanding of the above experimental results, the crack closure effect, transition condition and details of the growth mechanism are investigated.

From the perspective of crack closure, FCGR deceleration due to oxidation is also commonly reported for “long” fatigue cracks., J. Telesman et al. recently demonstrated that oxidation increases the ΔK_{th} level but accelerates the FCGR of the Paris region by investigating the effects of a vacuum environment, testing temperature and loading frequency on the “long” fatigue cracks seen in the Ni-Co based superalloys ME3 and LSHR [30]. They explained the change in ΔK_{th} level from the perspective of oxide-induced crack closure. It was noteworthy that our results demonstrated that similar positive oxidation effects on ΔK_{th} were also true for “small” fatigue cracks. This result is not as would be expected, because usually crack closure gradually grows along with crack growth [27,31,32]. We have successfully clarified that oxidation increases crack closure levels also for short fatigue cracks, as shown in Figure 12. However, according to quantitative evaluation of ΔK_{eff} using DIC, the crack closure level was not sufficiently to explain the difference in FCGR between RT and elevated temperatures as shown

in Fig. 13, since FCGRs at elevated temperatures in air were slower than the expected rate. In contrast, the differences in FCGR between “long” and “small” fatigue cracks at RT disappeared when using ΔK_{eff}. Hence the change in FCG mechanism due to oxidation should be also investigated to gain a quantitative understanding.

The FCG mode transition condition from slow TG FCG to fast IG FCG is potentially helpful for understanding the FCG mechanism. Here, the relationship between plastic zone size, microstructural size and transition point were evaluated as shown in Figure 17. The plastic zone size of the crack tip under plane strain condition assuming von Mises yielding criteria is expressed by following equations.

$$r_p = \frac{1}{2\pi}\left(\frac{K}{\lambda\sigma_y}\right)^2 \quad (1), \text{ and}$$

$$\lambda = \frac{1+sin\frac{\theta}{2}}{\sqrt{3\,sin^2\frac{\theta}{2}+(1-2\nu)^2}} \quad (2),$$

where K is the stress intensity factor, σ_y is the yielding strength, ν is Poisson’s ratio and θ is the angle from the loading plane. In this approach, plane strain conditions were assumed to evaluate the deepest point of the SFCs. The plastic zone size during the fatigue test was calculated using ΔK_{eff}, 0.2 % yielding strength at the testing temperature and $\theta = 72^{\circ}$. It note that ΔK_{eff} was used instead of K_{max} for this calculation because, as shown in Fig. 13, the transition point was related to ΔK_{eff} rather than K_{max} which is same as ΔK under $R = -1$. In addition, IG FCG mode possibly related to oxidation damage along grain boundary inside

the plastic zone. Hence $\theta = 72^{\circ}$ was used in consideration of zig-zag path of IG FCG. Figure 17 shows the FCG transition condition represented as number fractions of grain size distribution. As shown in Fig. 13, the FCG mode transition of the slow TG mode to the fast IG mode occurred around $\Delta K_{\mathrm{eff}} = 5$ - 7 MPa $\mathrm{m}^{0.5}$. The corresponding plastic zone size at the transition point was 3 - 5 μm. As shown in Fig. 17, this plastic zone size was close to the peak of the grain size number fraction. The oxidation damage inside the plastic zone that increases FCGR was noted in previous research [23,33]. It appears that oxygen transportation through the grain boundary and the damage due to the oxidation was enhanced inside the plastic zone. It is thus conceivable that the fast IG FCG mode dominates when the plastic zone covers the grain size.

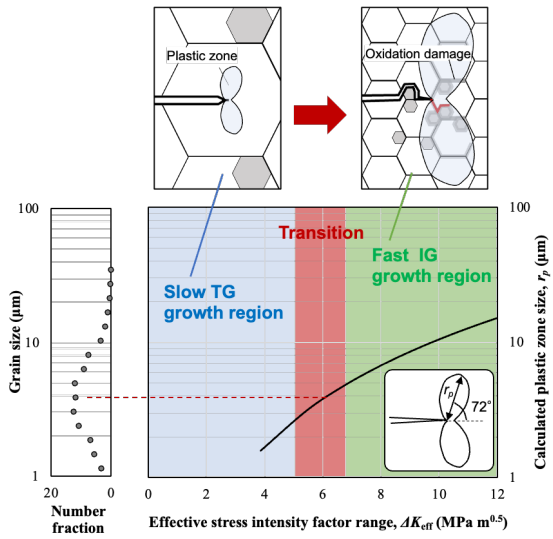

Figure 17. Schematic of SFCG modes transition states caused by oxidation

The details of the FCG mechanism, fast IG, and slow TG FCG mode will be discussed below. The abrupt FCGR acceleration in regions with large ΔK identified in this study is concluded to occur due to intergranular damage caused by oxidation. The FCGR acceleration accompanied by intergranular cracking was previously investigated for each long [10,11] and short fatigue crack [22]. According to the 3D investigation in Fig. 14, the intergranular (IG) crack region preceded the surrounding crack tip, but was connected to the main crack. It thus appears likely that IG cracks grow faster than in other areas and occur due to oxygen being transported from the crack tip. This fast IG FCG mechanism has been closely investigated in previous research [22,23,34].

On the other hand, there are no reports on the slow TG FCG mode or its mechanism in the small ΔK region. Telesman et al. reported the oxidation effect on ΔK_{th} [30], while the FCGRs in their tests were faster than in our experiment, as illustrated for comparison in Figure 13. Hence, they did not report the slow TG FCG mode. As shown in Fig. 14, slow TG FCG at elevated temperatures was governed by a completely different mechanism from that at room temperature. The SFCs at room temperature were growing along the {111} slip plane with shear stress as shown in Fig. 14 a). In contrast, the slow crack growth area at elevated temperature was insensitive to the microstructure and mostly grew perpendicular to the loading axis. This flat crack propagation area in Fig. 14 also shows an almost semicircular shape. It therefore appears as if crack growth is determined solely by mechanical conditions. Crack growth of this type possibly

occurred due to intermittent small embrittlement in the crack tip oxidation region. This apparent brittleness is reminiscent of the fast FCG mode in spite of the FCGR of this region being slower than the others. Plastic deformation around the crack tip might help to explain these curious phenomena.

As shown in Fig. 16, plastic deformation around the crack at elevated temperatures was more broadly distributed than at room temperature. However, the calculated crack tip plastic zone size at RT and elevated temperatures were comparable. According to Eq (1), (2) and the yielding strength at the tested temperatures, the plastic zone sizes in $\theta = 72^{\circ}$ were 8.6 and 5.6 μm, respectively, at RT and at elevated temperatures. Here, fatigue crack essentially grows due to the newly formed surface at the crack tip generated by slip deformation [35]. Hence, only dislocations emitted from the crack tip contribute to fatigue crack extension. For example, Takahashi et al. proposed dislocation based FCG model which explain FCGR acceleration due to the concentration of dislocation emission at the crack tip [36]. In other words, plastic deformation at a distance from the crack tip does not expand the crack. If the total plastic deformation around the crack tip is related to the calculated plastic zone size, slip deformation at room temperature appears to be more concentrated at the crack tip than under elevated temperature conditions. It appears likely that the broadly distributed apparent plastic zone at elevated temperatures, shown in Fig. 16, does not contribute to crack extension. In other words, slip deformation at the crack tip at elevated temperatures appears to be smaller than that at room temperature. Slip

deformation at the crack tip might be interrupted by the oxidation layer. According to previous studies, oxidation layer of Ni-Co based superalloy consisted of NiO, CoO, Cr_2O_3, TiO_2 and Al_2O_3 [37,38]. The last three of these oxides were formed along the flanks of the fatigue crack [38]. Such oxides are usually harder than bulk material [39] while Young's modulus of oxide layer was comparable to base metal [40]. Such a hard oxide layer on the crack surface possibly interrupt the dislocation emission from the crack tip. This may be one reason why the FCGR at elevated temperatures was slower than at room temperature, even if using ΔK_{eff}. However, the microscopic detail for the character of oxides around the crack tip was not clarified in this study. For example, nanoscopic segregation along grain boundaries [41] possibly affects the FCG mode transition behavior. This is the next issue of this study.

The schematics of the FCG process with and without oxidation, assuming the above, are described in Figure 18. As shown in Fig. 18 a_1), fatigue cracks grow along the slip plane in the first part of the fatigue process in the absence of oxidation. Although the observation in Fig. 14 was the result for RT, a similar mechanism appears to apply at elevated temperatures in a vacuum, since similar facets were observed on fatigue fracture surfaces under vacuum. This process is similar to the crack initiation mechanism [42] except that this process continued past a surface crack length of 0.3 mm. The usual TG FCG process [35,43], shown in Fig. 15 a_2), accompanied by fatigue striations, therefore appears to apply in larger ΔK regions. Figure 18 b) shows the schematics of SFCG under

oxidation. As shown in Fig. 18 b_1), SFC appears to grow inside the oxide layer in a brittle manner, driven by the principal stress at the crack tip. It should be noted that the oxide-induced crack closure of this region was confirmed in our experiments, but was not sufficient to explain slow FCGR at elevated temperatures. It appears that not the crack tip itself, but areas distant from the tip which do not contribute to crack extension undergo plastic deformation of the plastic zone, possibly due to the inhibition, by the oxidation layer, of dislocation emissions from the crack tip. This slow FCG process could be a unique and hitherto unreported process. It then transits to the IG FCG mode shown in Fig. 18 b_2) when the plastic zone covers the grain size as described in Figure 17.

In summary, FCGR deceleration in the small ΔK region and acceleration in the large ΔK region due to oxidation were observed during the SFCG process of TMW4M3 superalloy. FCGR differences due to oxidation could not be explained solely by crack closure. Our three-dimensional investigation suggests that changes in slip deformation mode due to the oxide layer in the crack tip play an important role in FCGR deceleration in the small ΔK region.

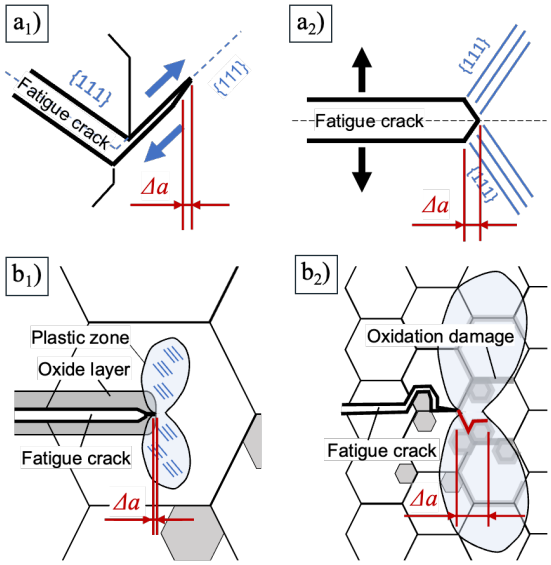

Figure 18. Schematics of the SFCG modes for a) without oxidation and b) with oxidation. a_1) and b_1) show the first part and a_2) and b_2) show the latter part of the fatigue process.

5. Conclusion

In this research, to elucidate the oxidation effect on SFCG characteristics of Ni-Co based TMW-4M3 superalloy, we conducted fatigue tests in air/vacuum at elevated temperatures, *in situ* observation of SFCG behaviour in air at room/elevated temperature which include the SFCs opening/closing behaviour, and three-dimensional microscopic observations of the SFCs using a PFIB – SEM system. The following conclusions can be drawn from our results.

1. The fatigue lives tested under vacuum at elevated temperatures were comparable to those at room temperature. In contrast, those tested at elevated temperatures in air showed a shorter fatigue life in higher-stress regions and a longer fatigue life in lower-stress regions than the others.
2. *In situ* fatigue observations revealed SFCG deceleration in the small ΔK regions and acceleration in the large ΔK regions. Non-propagating fatigue cracks were observed in the specimen at the fatigue limit at elevated temperatures in air. The slow FCGR region showed flat TG fracture surfaces, and fast regions showed blocky IG fracture surfaces.
3. The opening/closing behaviours of SFCs at elevated temperature were successfully measured using DIC. The crack opening stress was increased at elevated temperatures in air, possibly due to oxide-induced crack closure. However, the difference in FCGR between room and elevated temperatures in air cannot be explained solely by crack closure effects.

4. Three-dimensional investigations revealed a completely different SFCG mechanism at room and at elevated temperatures in air. The SFCs at elevated temperatures showed straight TG FCG to be insensitive to the microstructure in slow growth regions and that IG FCG precedes the surroundings in acceleration regions in contrast to microstructural SFCG features at room temperature. The apparent plastic zone at elevated temperatures was also more broadly distributed than that at room temperature despite the calculated values being comparable.
5. It appears that slow and straight SFCG at elevated temperatures occurs due to intermittent brittle fracture of the oxide that forms at the crack tip. The oxide layer of the crack tip likely acts to broaden the plastic deformation distribution, which in turn contributes to FCGR deceleration.

Acknowledgments

This research was supported by the Council for Science, Technology and Innovation (CSTI), the Cross-ministerial Strategic Innovation Promotion Program (SIP), "Materials Integration" for Revolutionary Design Systems for Structural Materials (Funding agency: JST). The PFIB - SEM observations were performed by Ms. Y. Hara. We also would like to thank Mr. Takukma Kohata for assistance with the SEM observations.

Data availability

The raw/processed data required to reproduce these findings cannot be shared at this time due to technical or time limitations.

References

[1] R.C. Reed, The Superalloys: Fundamentals and Applications, Cambridge University Press, Cambridge, 2006. doi:DOI: 10.1017/CBO9780511541285.

[2] Y. Gu, H. Harada, C. Cui, D. Ping, A. Sato, J. Fujioka, New Ni-Co-base disk superalloys with higher strength and creep resistance, Scr. Mater. 55 (2006) 815–818. doi:10.1016/j.scriptamat.2006.07.008.

[3] Y.F. Gu, T. Osada, T. Yokokawa, H. Harada, J. Fujioka, D. Nagahama, M. Okuno, Development of nickel-cobalt base P/M superalloys for disk applications, Proc. Int. Symp. Superalloys. 2016-Janua (2016) 209–216. doi:10.1002/9781119075646.ch23.

[4] J. Fujioka, Y.F. Gu, T. Osada, C.Y. Cui, T. Kobayashi, T. Yokokawa, H. Harada, T. Fukuda, A. Mitsuhashi, Development of Ni-Co-base superalloys based on new concept for high temperature turbine disk applications, Proc. Int. Gas Turbine Congr. 2015 Tokyo. (2015) 333–338.

[5] C.Y. Cui, Y.F. Gu, H. Harada, D.H. Ping, A. Sato, Phase stability and yield stress of Ni-base superalloys containing high Co and Ti, Metall. Mater. Trans. A Phys. Metall. Mater. Sci. 37 (2006) 3183–3190. doi:10.1007/BF02586152.

[6] Y.F. Gu, C. Cui, D. Ping, H. Harada, T. Fukuda, J. Fujioka, Creep behavior of new kinds of Ni-Co-base superalloys, Mater. Sci. Eng. A. 510–511 (2009) 250–255. doi:10.1016/j.msea.2008.04.128.

[7] T. Osada, Y. Gu, N. Nagashima, Y. Yuan, T. Yokokawa, H. Harada, Optimum microstructure combination for maximizing tensile strength in a polycrystalline superalloy with a two-phase structure, Acta Mater. 61 (2013) 1820–1829. doi:10.1016/j.actamat.2012.12.004.

[8] Anvari, Failure of Nickel-based super alloy (ME3) in aerospace gas turbine engines, J. Chem. Eng. Mater. Sci. 8 (2017) 46–65. doi:10.5897/jcems2016.0282.

[9] R.S.J. Corran, S.J. Williams, Lifing methods and safety criteria in aero gas turbines, Eng. Fail. Anal. 14 (2007) 518–528. doi:10.1016/j.engfailanal.2005.08.010.

[10] Z. Zhong, Y. Gu, Y. Yuan, C. Cui, T. Yokokawa, H. Harada, Fatigue crack growth behavior of a newly developed Ni-Co-base superalloy TMW-2 at elevated temperatures, Mater. Sci. Eng. A. 552 (2012) 464–471. doi:10.1016/j.msea.2012.05.071.

[11] Z. Zhong, Y. Gu, T. Osada, Y. Yuan, C. Cui, T. Yokokawa, T. Tetsui, H. Harada, Fatigue crack growth characteristics of a new Ni-Co-base superalloy TMW-4M3: Effects of temperature and load ratio, J. Mater. Sci. 46 (2011) 7573–7581. doi:10.1007/s10853-011-5732-0.

[12] Z. Zhong, Y. Gu, Y. Yuan, T. Yokokawa, H. Harada, On the low cycle fatigue behavior of a Ni-base superalloy containing high Co and Ti contents, Mater. Sci. Eng. A. 552 (2012) 434–443. doi:10.1016/j.msea.2012.05.067.

[13] Z. Zhong, Y. Gu, Y. Yuan, T. Osada, C. Cui, T. Yokokawa, T. Tetsui, H. Harada, Effect of solution temperature on the microstructure and mechanical properties of a newly developed superalloy TMW-4M3, Metall. Mater. Trans. A Phys. Metall. Mater. Sci. 43 (2012) 1017–1025. doi:10.1007/s11661-011-0926-2.

[14] R.O. Ritchie, J. Lankford, Small fatigue cracks: A statement of the problem and potential solutions, Mater. Sci. Eng. 84 (1986) 11–16. doi:10.1016/0025-5416(86)90217-X.

[15] K.J. Miller, Materials science perspective of metal fatigue resistance, Mater. Sci. Technol. 9 (1993) 453–462. doi:10.1179/mst.1993.9.6.453.

[16] M. Okada, M. Tsutsumi, T. Kitamura, R. Ohtani, INITIATION AND GROWTH OF SMALL CRACKS IN DIRECTIONALLY SOLIDIFIED MAR-M247 UNDER CREEP-FATIGUE. PART I: EFFECT OF MICROSTRUCTURE, Fatigue Fract. Eng. Mater. Struct. 21 (1998) 741–750. doi:https://doi.org/10.1046/j.1460-2695.1998.00540.x.

[17] M. Okada, M. Tsutsumi, T. Kitamura, R. Ohtani, INITIATION AND GROWTH OF SMALL CRACKS IN DIRECTIONALLY SOLIDIFIED

MAR-M247 UNDER CREEP-FATIGUE PART II: EFFECT OF ANGLE NETWEEN STRESS AXIS AND SOLIDIFICATION DIRECTION, Fatigue Fract. Eng. Mater. Struct. 21 (1998) 751–760. doi:https://doi.org/10.1046/j.1460-2695.1998.00454.x.

[18] J.C. Healy, L. Grabowski, C.J. Beevers, Short-fatigue-crack growth in a nickel-base superalloy at room and elevated temperature, Int. J. Fatigue. 13 (1991) 133–138. doi:10.1016/0142-1123(91)90005-J.

[19] R.A. Smith, Y. Liu, L. Grabowski, SHORT FATIGUE CRACK GROWTH BEHAVIOUR IN WASPALOY AT ROOM AND ELEVATED TEMPERATURES, Fatigue Fract. Eng. Mater. Struct. 19 (1996) 1505–1514. doi:https://doi.org/10.1111/j.1460-2695.1996.tb00185.x.

[20] A.H. Rosenberger, H. Ghonem, HIGH TEMPERATURE ELASTIC-PLASTIC SMALL CRACK GROWTH BEHAVIOR IN A NICKEL-BASE SUPERALLOY, Fatigue Fract. Eng. Mater. Struct. 17 (1994) 509–521. doi:https://doi.org/10.1111/j.1460-2695.1994.tb00251.x.

[21] M.J. Caton, S.K. Jha, Small fatigue crack growth and failure mode transitions in a Ni-base superalloy at elevated temperature, Int. J. Fatigue. 32 (2010) 1461–1472. doi:10.1016/j.ijfatigue.2010.01.015.

[22] R. Jiang, D. Proprentner, M. Callisti, B. Shollock, X.T. Hu, Y.D. Song, P.A.S. Reed, Role of oxygen in enhanced fatigue cracking in a PM Ni-

based superalloy: Stress assisted grain boundary oxidation or dynamic embrittlment?, Corros. Sci. 139 (2018) 141–154. doi:10.1016/j.corsci.2018.05.001.

[23] R. Jiang, Y.D. Song, P.A. Reed, Fatigue crack growth mechanisms in powder metallurgy Ni-based superalloys—A review, Int. J. Fatigue. 141 (2020) 105887. doi:10.1016/j.ijfatigue.2020.105887.

[24] E. Wolf, Fatigue crack closure under cyclic tension, Eng. Fract. Mech. 2 (1970) 37–45. doi:https://doi.org/10.1016/0013-7944(70)90028-7.

[25] H. Nishikawa, Y. Furuya, Development of a Method for Evaluating Microstructurally Small Fatigue Crack Initiation and Growth by Using an Automatic System for *In Situ* Observation in Conjunction with a Digital-Image Correlation Technique, ISIJ Int. 60 (2020) 2090–2096. doi:10.2355/isijinternational.ISIJINT-2019-823.

[26] H. Nishikawa, Y. Furuya, T. Osada, K. Kawagishi, T. Hara, Three-dimensional high-resolution crystallographic observation of the entire volume of microstructurally small fatigue cracks in Ni-Co based superalloy, Scr. Mater. 222 (2023) 115026. doi:10.1016/j.scriptamat.2022.115026.

[27] H. Ito, Y. Suzuki, H. Nishikawa, M. Kinefuchi, M. Enoki, K. Shibanuma, Multiscale model prediction of ferritic steel fatigue strength based on microstructural information , tensile properties , and loading conditions

(no adjustable material constants), Int. J. Mech. Sci. 170 (2020) 105339. doi:10.1016/j.ijmecsci.2019.105339.

[28] K. Habib, H. Nishikawa, Y. Furuya, S. Emura, The Role of Crystallographic Texture and Basal Plane Slip on Microstructurally Short Fatigue Crack Initiation and Propagation in Forged Billet and Rolled Bar Ti-6Al-4V Alloy, Metall. Mater. Trans. A. 52 (2021) 3821–3838. doi:10.1007/s11661-021-06344-z.

[29] ASTM E647 Standard Test Method for Measurement of Fatigue Crack Growth Rates, ASTM International, West Conshohocken, PA, 2023.

[30] J. Telesman, T.M. Smith, T.P. Gabb, A.J. Ring, An Abrupt Transition to an Intergranular Failure Mode in the Near-Threshold Fatigue Crack Growth Regime in Ni-Based Superalloys, Metall. Mater. Trans. A Phys. Metall. Mater. Sci. 49 (2018) 3838–3853. doi:10.1007/s11661-018-4685-1.

[31] S. Suresh, R.O. Ritchie, Propagation of short fatigue cracks, Int. Met. Rev. 29 (1984) 445–473. doi:10.1179/imtr.1984.29.1.445.

[32] A.J. McEvily, K. Minakawa, Crack closure and the growth of short and long fatigue cracks, Scr. Metall. 18 (1984) 71–76. doi:10.1016/0036-9748(84)90092-9.

[33] R. Jiang, D.J. Bull, D. Proprentner, B. Shollock, P.A.S. Reed, Effects of oxygen-related damage on dwell-fatigue crack propagation in a P/M Ni-

based superalloy: From 2D to 3D assessment, Int. J. Fatigue. 99 (2017) 175–186. doi:10.1016/j.ijfatigue.2017.03.003.

[34] S. Suzuki, M. Sakaguchi, M. Domen, T. Karato, K. Suzuki, Temperature and ΔK dependence of grain boundary effect on fatigue crack propagation in a two-dimensional polycrystalline Ni-base superalloy, Acta Mater. 240 (2022) 118288. doi:10.1016/j.actamat.2022.118288.

[35] P. Neumann, New experiments concerning the slip processes at propagating fatigue cracks-I, Acta Metall. 22 (1974) 1155–1165. doi:10.1016/0001-6160(74)90071-6.

[36] Y. Takahashi, M. Tanaka, K. Higashida, K. Yamaguchi, H. Noguchi, An intrinsic effect of hydrogen on cyclic slip deformation around a {1 1 0} fatigue crack in Fe-3.2 wt.% Si alloy, Acta Mater. 58 (2010) 1972–1981. doi:10.1016/j.actamat.2009.11.040.

[37] C.K. Sudbrack, S.L. Draper, T.T. Gorman, J. Telesman, T.P. Gabb, D.R. Hull, Oxidation and the Effects of High Temperature Exposures on Notched Fatigue Life of an Advanced Powder Metallurgy Disk Superalloy, Superalloys 2012. (2012) 863–872. doi:10.1002/9781118516430.ch95.

[38] H.S. Kitaguchi, H.Y. Li, H.E. Evans, R.G. Ding, I.P. Jones, G. Baxter, P. Bowen, Oxidation ahead of a crack tip in an advanced Ni-based superalloy, Acta Mater. 61 (2013) 1968–1981. doi:10.1016/j.actamat.2012.12.017.

[39] F.S. Ahmed, M.A. El-Zomor, M.S.A. Ghazala, R.N. Elshaer, Impact of thermal oxidation parameters on micro-hardness and hot corrosion of Ti-6Al-3Mo-2Nb-2Sn-2Zr-1.5Cr alloy, Sci. Rep. 13 (2023) 11249. doi:10.1038/s41598-023-38216-4.

[40] J. Everaerts, E. Salvati, H. Li, W. Li, A.M. Korsunsky, Mechanical properties of thermally grown submicron oxide layers on a nickel-based superalloy, Corros. Sci. 165 (2020) 108388. doi:10.1016/j.corsci.2019.108388.

[41] V. Mazánová, M. Heczko, J. Polák, Fatigue crack initiation and growth in 43Fe-25Ni-22.5Cr austenitic steel at a temperature of 700 °C, Int. J. Fatigue. 114 (2018) 11–21. doi:10.1016/j.ijfatigue.2018.04.033.

[42] K. Katagiri, A. Omura, K. Koyanagi, J. Awatani, T. Shiraishi, H. Kaneshiro, Early stage crack tip dislocation morphology in fatigued copper, Metall. Trans. A. 8 (1977) 1769–1773. doi:10.1007/BF02646881.

[43] R.M.N. Pelloux, Crack extension by alternating shear, Eng. Fract. Mech. 1 (1970) 697–704. doi:https://doi.org/10.1016/0013-7944(70)90008-1.